INTERNATIONAL JOURNAL FOR NUMERICAL METHODS IN FLUIDS
Int. J. Numer. Meth. Fluids 2007; **54**:1451–1471
Published online 31 January 2007 in Wiley InterScience (www.interscience.wiley.com). DOI: 10.1002/fld.1432

A stabilized finite element method for shape optimization in low Reynolds number flows

D. N. Srinath and S. Mittal*, †

Department of Aerospace Engineering, Indian Institute of Technology Kanpur, Kanpur, UP 208 016, India

SUMMARY

A gradient-based optimization procedure based on a continuous adjoint approach is formulated and implemented for steady low Reynolds number flows. A stabilized finite element formulation is proposed to solve the adjoint equations. The accuracy of the gradients from the adjoint approach is verified against the ones computed from a simple finite difference procedure. The validation of the formulation and its implementation is carried out *via* flow past an elliptical bump whose eccentricity is used as a design parameter. Shape design studies for the elliptical bump are then carried on with a more complex 4th order Bézier parametrization of the bump. Results for, both, optimal design and inverse problems are presented. Using different initial guesses, multiple optimal shapes are obtained. A multi-objective function with additional constraints on the volume and the drag coefficient of the bump is utilized. It is seen that as more constraints are added to the objective function the design space is constrained and the multiple optimal shapes become progressively similar to each other. The study demonstrates the usefulness of this tool in obtaining multiple engineering solutions to a given design problem and also providing a framework to impose multiple constraints simultaneously. Copyright © 2007 John Wiley & Sons, Ltd.

Received 15 August 2006; Revised 11 November 2006; Accepted 15 November 2006

KEY WORDS: shape optimization; adjoint methods; finite elements; multiple solutions; fluid flow

1. INTRODUCTION

Optimization methods can be broadly classified as one of the two types: global and local [1]. Global methods rely on random search to determine global optima of a predefined objective function. Some examples of such methods are genetic algorithms, simulated annealing, etc. Though extremely robust, these methods require a large number of objective function evaluations. In certain cases where each function evaluation is time consuming, these methods may become very expensive. Local search methods, on the other hand, are capable of determining only the local optima of the

*Correspondence to: S. Mittal, Department of Aerospace Engineering, Indian Institute of Technology Kanpur, Kanpur, UP 208 016, India.
†E-mail: smittal@iitk.ac.in

objective function. In these methods the search direction is based on the gradient of the objective function with respect to the identified design parameters.

For viscous flows, each evaluation of the objective function can be fairly time consuming. Therefore, gradient-based local methods are utilized in the present work. Different methods exist to calculate the gradient of the objective function. The complex Taylor series expansion approach [2–5], and the automatic- [6–8] and direct-differentiation [9] method can be employed to calculate the gradient of the objective function. Another possible approach is *via* a simple finite difference procedure. The flow is computed for a design variable and a small perturbation around it. These two points can now be used to compute the objective function and the gradient. Adjoint-based methods [10, 11] are usually preferred as they offer an economical framework to work with a large number of design variables. Pironneau [12, 13] proposed an optimal shape design algorithm and derived the optimality conditions to minimize the drag on a body in low Reynolds number laminar flow. For Stokes flow it was shown analytically that the minimum drag condition requires the magnitude of the normal derivative of the velocity to be constant on the surface of the body. Jameson [14] further developed this method for the Euler and the Navier–Stokes equations. In these methods, the objective function is augmented with the flow equations as constraint conditions *via* Lagrange Multipliers.

Based on the order of discretization and derivation of the adjoint equations, the adjoint-based methods can be further classified as continuous *vs* discrete. In the continuous adjoint method, the variation of the augmented objective function is derived first and then the resulting equations are discretized. In the discrete adjoint methods the discretization precedes the variation. Since the operations of discretization and variation do not commute, the gradients obtained with the two methods are not identical. However, as the grid spacing approaches zero, results from both the discrete and the continuous methods become closer. The advantage of the continuous adjoint method is that it is independent of the method used to solve the flow equations. Comparison of the two approaches can be found in [15, 16].

Adjoint-based optimization strategies have been used by various researchers in the past [17–25]. A survey of the recent developments in optimal shape design can be found in the review article by Mohammadi and Pirroneau [26]. Abraham *et al.* [27, 28] carried out shape optimization in the context of non-Newtonian fluids using stabilized finite element methods. Yagi and Kawahara [29] utilized shape optimization to achieve drag reduction in Stokes flow. They obtained a body on which the normal derivative of the velocity is constant, thereby satisfying the Pirroneau condition [12]. Okumura and Kawahara [30] utilized an optimization procedure to reduce the drag of a body in a $Re = 200$ flow. Starting from a circular cylinder the final shape is almost a flat surface.

In this paper an optimization procedure for steady incompressible flows using a continuous adjoint method is proposed and implemented. A new stabilized finite element formulation is proposed for solving the adjoint equations. It is based on the streamline-upwind Petrov/Galerkin (SUPG) and pressure-stabilizing Petrov/Galerkin (PSPG) stabilization techniques [31]. The minimization of the objective function is carried out by using the limited memory-Broyden–Fletcher–Goldfarb–Shanno (L-BFGS) algorithm [32]. The implementation is tested *via* optimizing the shape of a bump to achieve desired lift and drag coefficients. The bump is modelled as one-half of an ellipse; its eccentricity (ratio of minor to major axis) is used as a shape parameter. An unstructured grid is utilized to accommodate complex geometries that may arise in certain flow problems. A mesh moving scheme is employed to generate grids for the updated geometries. The validated implementation is employed to determine shapes of bumps with more design variables. The bump is modelled by a 4th order Bézier curve [33]. Drag minimization, as expected, results in an almost

DOI: 10.1002/fld

flat surface. The existence of several shapes that satisfy an objective function is illustrated *via* minimization of the magnitude of lift coefficient. These different shapes are realized by starting the optimization cycle with different initial geometries. Imposition of additional constraints, on volume and drag coefficient, progressively narrows the design space.

2. GOVERNING EQUATIONS

2.1. Flow equations

Consider a domain Ω, with boundary Γ, that is occupied by a fluid of density ρ and dynamic viscosity μ. The governing equations for a steady incompressible flow of this fluid are given as

$$\rho\mathbf{u}\cdot\nabla\mathbf{u}+\nabla\cdot\boldsymbol{\sigma}=\mathbf{f} \quad \text{on } \Omega \tag{1}$$

$$\nabla\cdot\mathbf{u}=0 \quad \text{on } \Omega \tag{2}$$

where $\mathbf{u}$ is the velocity, $\boldsymbol{\sigma}$ the stress tensor and $\mathbf{f}$ the body force. For a Newtonian fluid the stress tensor is given as $\boldsymbol{\sigma} = -p\mathbf{I}+\mu[\nabla\mathbf{u}+(\nabla\mathbf{u})^{\mathrm{T}}]$ where p is the pressure and $\mathbf{I}$ the identity tensor. The boundary conditions are either on the flow velocity or stress. Both, Dirichlet and Neumann-type boundary conditions are accounted for

$$\mathbf{u}=\mathbf{g} \quad \text{on } \Gamma_g \tag{3}$$

$$\mathbf{n}\cdot\boldsymbol{\sigma}=\mathbf{h} \quad \text{on } \Gamma_h \tag{4}$$

where $\mathbf{n}$ is the unit normal vector on the boundary Γ. Here, Γ_g and Γ_h are the subsets of the boundary Γ. More details on the boundary conditions are given in Figure 1. The drag and lift force, (D, L), on the body can be calculated using the following expression:

$$(D, L)=\int_{\Gamma_{\mathrm{B}}}\boldsymbol{\sigma}\mathbf{n}\,\mathrm{d}\Gamma \tag{5}$$

where Γ_{B} represents the surface of the body.

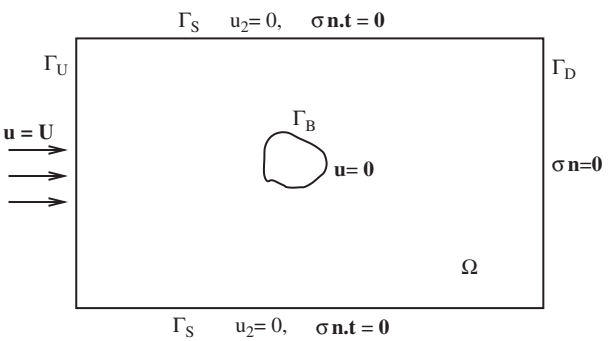

Figure 1. Schematic of the problem set-up: boundary conditions. Γ_{U}, Γ_{D} and Γ_{S} are the upstream, downstream and lateral boundaries, respectively, and Γ_{B} is the body surface.

DOI: 10.1002/fld

2.2. The continuous adjoint approach

Let Γ_B be the segment of the boundary, Γ, whose shape is to be determined. Let $\boldsymbol{\beta} = (\beta_1, \ldots, \beta_m)$ be the set of shape parameters that govern its shape. Further, an objective function, $I_c(\mathbf{U}, \boldsymbol{\beta})$, is defined that depends on the flow variables $\mathbf{U} = (\mathbf{u}, p)$ and shape parameters $\boldsymbol{\beta}$. The optimization problem involves determining the shape parameters that minimize (or maximize) the objective function, $I_c(\mathbf{U}, \boldsymbol{\beta})$.

The flow equations (1) and (2) may be written as $\mathfrak{R} = (\mathfrak{R}_\mathbf{u}, \Re_p)$, where $\mathfrak{R}_\mathbf{u}$ is the momentum equation and $\Re_p$ the continuity equation. These equations have to be satisfied for the flow variables $\mathbf{U} = (\mathbf{u}, p)$ that minimize (or maximize) the objective function, $I_c(\mathbf{U}, \boldsymbol{\beta})$. Therefore, the flow equations seem to appear as constraint conditions on the objective function. An augmented objective function is constructed to convert the constrained problem to an unconstrained one. The flow equations are augmented to the original objective function by introducing a set of Lagrange multipliers or adjoint variables, $\boldsymbol{\Psi} = (\boldsymbol{\psi}_\mathbf{u}, \psi_p)$

$$I = I_c + \int_\Omega \Psi \cdot \mathfrak{R} \, \mathrm{d}\Omega \tag{6}$$

It can be noticed that the augmented objective function degenerates to the original one if the flow variables, $\mathbf{U}$, satisfy Equations (1) and (2). Using principles of variational calculus, the variation of the augmented objective function is calculated as

$$\delta I = \frac{\partial I}{\partial \mathbf{U}} \delta \mathbf{U} + \frac{\partial I}{\partial \boldsymbol{\beta}} \delta \boldsymbol{\beta} + \frac{\partial I}{\partial \boldsymbol{\Psi}} \delta \boldsymbol{\Psi} \tag{7}$$

It is seen from Equation (7) that δI depends on variations of $\mathbf{U}$, $\boldsymbol{\beta}$ and $\boldsymbol{\Psi}$. These variations are given as

$$\frac{\partial I}{\partial \boldsymbol{\Psi}} = \mathfrak{R}(\mathbf{U}, \boldsymbol{\beta}) \tag{8}$$

$$\frac{\partial I}{\partial \mathbf{U}} = \left(\frac{\partial I_c}{\partial \mathbf{U}} + \int_\Omega \boldsymbol{\Psi}^\mathrm{T} \frac{\partial \mathfrak{R}}{\partial \mathbf{U}} \, \mathrm{d}\Omega \right) \tag{9}$$

$$\frac{\partial I}{\partial \boldsymbol{\beta}} = \left(\frac{\partial I_c}{\partial \boldsymbol{\beta}} + \int_\Omega \boldsymbol{\Psi}^\mathrm{T} \frac{\partial \mathfrak{R}}{\partial \boldsymbol{\beta}} \, \mathrm{d}\Omega \right) \tag{10}$$

The optimal solution is achieved when the variation of the augmented objective function vanishes, i.e. $\delta I = 0$. For this equation to be satisfied, the derivative of I with respect to each of the three parameters, i.e. the expressions in relations (8)–(10) should go to zero. Relation (8) leads to the flow equations (1) and (2). Relation (9) results in the adjoint equations which can be utilized to compute the adjoint field. More details are given in the next section. The gradient of the augmented objective function, as given by relation (10), quantifies the sensitivity of the objective function with respect to the design parameters. It is utilized to refine the direction of search of the optimal shape parameters. The optimal solution is obtained when the gradient approaches zero.

DOI: 10.1002/fld

2.3. Adjoint equations

The equations and the boundary conditions for the adjoint variables are obtained by setting the expression given in (9) to zero. This leads to

$$\rho(\nabla\mathbf{u})^{\mathrm{T}}\boldsymbol{\psi}_{\mathbf{u}} - \rho(\mathbf{u}\cdot\nabla)\boldsymbol{\psi}_{\mathbf{u}} - \nabla\cdot\boldsymbol{\sigma}_{\boldsymbol{\psi}} = \mathbf{0} \quad \text{on } \Omega \tag{11}$$

$$\nabla\cdot\boldsymbol{\psi}_{\mathbf{u}} = 0 \quad \text{on } \Omega \tag{12}$$

where $\boldsymbol{\sigma}_{\boldsymbol{\psi}}$ is similar to the stress tensor and is given by $\boldsymbol{\sigma}_{\boldsymbol{\psi}} = -\psi_p\mathbf{I} + \mu[\nabla\boldsymbol{\psi}_{\mathbf{u}} + (\nabla\boldsymbol{\psi}_{\mathbf{u}})^{\mathrm{T}}]$. The variables $\boldsymbol{\psi}_{\mathbf{u}}$ and ψ_p are referred to as the adjoint velocity and adjoint pressure, respectively. Unlike the flow equations the equations for the adjoint variables are linear. The boundary conditions on the adjoint variables are

$$\boldsymbol{\psi}_{\mathbf{u}} = \mathbf{0} \quad \text{on } \Gamma_{\mathrm{U}} \tag{13}$$

$$\mathbf{s} = \mathbf{0} \quad \text{on } \Gamma_{\mathrm{D}} \tag{14}$$

$$s_1 = 0, \quad \psi_{u2} = 0 \quad \text{on } \Gamma_{\mathrm{S}} \tag{15}$$

$$-\int_{\Gamma_{\mathrm{B}}} \delta(\boldsymbol{\sigma}\cdot\mathbf{n})\cdot\boldsymbol{\psi}_{\mathbf{u}}\,\mathrm{d}\Gamma\,\mathrm{d}t + \frac{\partial I_c}{\partial\mathbf{u}}\delta\mathbf{u} + \frac{\partial I_c}{\partial p}\delta p = \mathbf{0} \quad \text{on } \Gamma_{\mathrm{B}} \tag{16}$$

where $\mathbf{s} = \{\mathbf{u}\boldsymbol{\psi}_{\mathbf{u}} - \psi_p + \mu[\nabla\boldsymbol{\psi}_{\mathbf{u}} + (\nabla\boldsymbol{\psi}_{\mathbf{u}})^{\mathrm{T}}]\}\cdot\mathbf{n}$. Γ_{U}, Γ_{D} and Γ_{S} are the upstream, downstream and lateral boundaries and Γ_{B} is the body surface (see Figure 1). The boundary conditions on the surface of the body depend on the definition of the objective function. This is illustrated with an example. Let $I_c = \frac{1}{2}C_{\mathrm{l}}^2$, where C_{l} is the coefficient of lift acting on the body. This objective function is useful in designing a body that yields minimum lift coefficient. In this case, it can be shown that, the boundary conditions for the adjoint variables on the body surface given by Equation (16) can be simplified to

$$\psi_{u1} = 0 \quad \text{on } \Gamma_{\mathrm{B}} \tag{17}$$

$$\psi_{u2} = C_{\mathrm{l}} \quad \text{on } \Gamma_{\mathrm{B}} \tag{18}$$

3. FINITE ELEMENT FORMULATION

3.1. The flow equations

The domain Ω is discretized into subdomains Ω^e, $e = 1, 2, \ldots, n_{\mathrm{el}}$, where n_{el} is the number of elements. Let $\mathscr{S}_u^h$ and $\mathscr{S}_p^h$ be the appropriate finite element spaces and $\mathscr{V}_u^h$ and $\mathscr{V}_p^h$ the weighing function spaces for velocity and pressure, respectively. The stabilized finite element formulation of Equations (1) and (2) is written as follows: find $\mathbf{u}^h \in \mathscr{S}_u^h$ and $p^h \in \mathscr{S}_p^h$ such that $\forall \mathbf{w}^h \in \mathscr{V}_u^h$, $q^h \in \mathscr{V}_p^h$

$$\int_\Omega \mathbf{w}^h\cdot\rho(\mathbf{u}\cdot\nabla\mathbf{u} - \mathbf{f})\,\mathrm{d}\Omega + \int_\Omega \varepsilon(\mathbf{w}^h : \boldsymbol{\sigma}(p^h, \mathbf{u}^h))\,\mathrm{d}\Omega$$

$$+ \int_\Omega q^h\nabla\cdot\mathbf{u}^h\,\mathrm{d}\Omega + \sum_{e=1}^{n_{\mathrm{el}}}\int_{\Omega^e}\frac{1}{\rho}(\tau_{\mathrm{SUPG}}\rho\mathbf{u}^h\cdot\nabla\mathbf{w}^h + \tau_{\mathrm{PSPG}}\nabla q^h)$$

DOI: 10.1002/fld

$$\cdot\,[\rho(\mathbf{u}\cdot\nabla\mathbf{u}-\mathbf{f})-\nabla\cdot\boldsymbol{\sigma}]\,\mathrm{d}\Omega^e$$

$$+\sum_{e=1}^{n_{\mathrm{el}}}\int_{\Omega^e}\tau_{\mathrm{LSIC}}\nabla\cdot\mathbf{w}^h\rho\nabla\cdot\mathbf{u}^h\,\mathrm{d}\Omega^e=\int_{\Gamma^h}\mathbf{w}^h\cdot\mathbf{h}^h\,\mathrm{d}\Gamma \tag{19}$$

The first three terms and the right-hand side in the variational formulation given by Equation (19) constitute the Galerkin formulation of the problem. The terms involving the element level integrals are the stabilization terms added to the basic Galerkin formulation to enhance its numerical stability. These terms stabilize the computations against node-to-node oscillations in advection dominated flows and allow the use of equal-in-order basis functions for velocity and pressure. The terms with coefficients τ_{SUPG} and τ_{PSPG} are based on the SUPG and PSPG method [31]. The term with coefficient τ_{LSIC} is also a stabilization term based on the least squares of the incompressibility constraint and is found to be useful for large Reynolds number flows. Equal-in-order basis functions for velocity and pressure, that are linear in space (three-noded triangular elements) are used. A three point quadrature is employed for numerical integration.

3.2. The adjoint equations

A stabilized SUPG/PSPG finite element method is proposed to solve the adjoint equations (11) and (12). Let $\mathscr{S}^h_{\boldsymbol{\psi}_{\mathbf{u}}}$ and $\mathscr{S}^h_{\psi_p}$ be the appropriate finite element spaces and $\mathscr{V}^h_{\boldsymbol{\psi}_{\mathbf{u}}}$ and $\mathscr{V}^h_{\psi_p}$ the corresponding weighting function spaces for the adjoint velocity and adjoint pressure. The stabilized finite element formulation of Equations (11) and (12) is written as follows: given $\mathbf{u}^h$ and $\mathbf{p}^h$ satisfying Equations (1) and (2), find $\boldsymbol{\psi}^h_u\in\mathscr{S}^h_{\boldsymbol{\psi}_{\mathbf{u}}}$ and $\boldsymbol{\psi}^h_p\in\mathscr{S}^h_{\psi_p}$ such that $\forall\mathbf{w}^h_{\boldsymbol{\psi}_{\mathbf{u}}}\in\mathscr{V}^h_{\boldsymbol{\psi}_{\mathbf{u}}}$, $q^h_{\psi_p}\in\mathscr{V}^h_{\psi_p}$

$$\int_\Omega\mathbf{w}^h_{\boldsymbol{\psi}_{\mathbf{u}}}\cdot\rho((\nabla\mathbf{u}^{\mathbf{h}})^{\mathrm{T}}\boldsymbol{\psi}^h_{\mathbf{u}}-\mathbf{u}\cdot\nabla\boldsymbol{\psi}_{\mathbf{u}})\,\mathrm{d}\Omega+\int_\Omega\varepsilon(\mathbf{w}^h_{\boldsymbol{\psi}_{\mathbf{u}}}):\boldsymbol{\sigma}_{\boldsymbol{\psi}}(\psi^h_p,\boldsymbol{\psi}^h_{\mathbf{u}})\,\mathrm{d}\Omega$$

$$+\int_\Omega q^h_{\psi_p}\nabla\cdot\boldsymbol{\psi}^h_{\mathbf{u}}\,\mathrm{d}\Omega+\sum_{e=1}^{n_{\mathrm{el}}}\int_{\Omega^e}\frac{1}{\rho}(-\tau_{\mathrm{SUPG}}\rho\mathbf{u}^h\cdot\nabla\mathbf{w}^h_{\boldsymbol{\psi}_{\mathbf{u}}}+\tau_{\mathrm{PSPG}}\nabla q^h_{\psi_p})$$

$$\cdot\,[\rho((\nabla\mathbf{u}^{\mathbf{h}})^{\mathrm{T}}\boldsymbol{\psi}^h_{\mathbf{u}}-\mathbf{u}\cdot\nabla\boldsymbol{\psi}_{\mathbf{u}})-\nabla\cdot\boldsymbol{\sigma}_{\boldsymbol{\psi}}(\psi^h_p,\boldsymbol{\psi}^h_{\mathbf{u}})]\,\mathrm{d}\Omega^e$$

$$+\sum_{e=1}^{n_{\mathrm{el}}}\int_{\Omega^e}\tau_{\mathrm{LSIC}}\nabla\cdot\mathbf{w}^h_{\boldsymbol{\psi}_{\mathbf{u}}}\rho\nabla\cdot\boldsymbol{\psi}^h_{\mathbf{u}}\,\mathrm{d}\Omega^e=\mathbf{0} \tag{20}$$

The stabilization coefficients τ_{SUPG}, τ_{PSPG} and τ_{LSIC} in the formulation proposed in Equation (20) are computed based on the flow variables ($\mathbf{u}$, p).

4. IMPLEMENTATION OF THE OPTIMIZATION PROCEDURE

A brief description of the sequence of steps in implementing the optimization procedure is given in this section. First, an objective function, I_c is identified. Then, the boundary surface whose design is sought is parametrized by a set of design parameters, $\boldsymbol{\beta}$. Initial value of these set of parameters is assumed to generate a shape for initial guess. A finite element mesh is generated for this shape.

DOI: 10.1002/fld

Next, the flow equations given by (1) and (2) are solved to obtain the steady-state flow: ($\mathbf{u}$, p). The adjoint equations given by (11) and (12) along with the appropriate boundary conditions are solved next to give ($\boldsymbol{\psi}_{\mathbf{u}}$, ψ_p). Next, Equation (10) is utilized to evaluate the gradient of the augmented objective function with respect to each design parameter. The gradient is an indication of how far/close one is to the optimal design. The gradient information is passed to an optimization routine that utilizes these values to search the update direction for the design parameters. The corrected shape parameters are now used to obtain the updated geometry. The entire procedure is repeated till the norm of the gradient vector falls below a certain preset threshold value. Unless stated otherwise the value of gradient reported in this paper corresponds to the L^2 norm of the vector $\partial I/\partial \boldsymbol{\beta}$. In this work, the linear equation systems resulting from the finite element discretization of the flow and the adjoint equations are solved using a direct method. This is based on the LU decomposition of the matrix and utilizing its sky-line structure. For unsteady and large-scale problems, one may use iterative solution techniques to reduce computational effort.

4.1. The optimizer

The optimization algorithm used in the present work is the L-BFGS procedure [32]. This is a limited memory algorithm for solving large non-linear optimization problems that are constrained by upper and lower bounds on the design variables. This algorithm is well suited for problems in which the information for the second derivative (the Hessian) is difficult to obtain.

4.2. Mesh movement strategy

In the optimization cycle the shape of the surface changes after each iteration. One possible method to handle this situation is to remesh after each iteration. Although this type of an implementation works for any arbitrary-shaped body and deformations, there are certain disadvantages. It can be computationally quite expensive and for unsteady flows may lead to projection errors. For steady flow, the projection of solution from one iteration to the other can lead to slower convergence of the non-linear flow equations. In the present work, a mesh moving scheme is employed. A finite element mesh is generated for the initial geometry. The nodes are subsequently relocated to conform to the changing shapes while retaining the connectivity between them. The computational domain is modelled as a linearly elastic solid. To reduce distortion of the mesh the smaller elements are made stiffer. The modified equations of linear elasticity are solved for the internal nodal displacements based on the given shape deformation of the solid boundary. More details about this procedure can be found in the article by Tezduyar *et al.* [34]. If the resulting mesh is associated with unacceptable levels of element distortion one has the option to generate a new mesh.

4.3. Parametrization

The parametrization of the shape decides the choice of the design variables. It should be simple and inexpensive while still offering a rich family of shapes so that the final design is useful. In the present work Bézier curves [33] have been used to parametrize the surface. Although more flexible and sophisticated options for defining the surface are available, Bézier curves are easy to implement. For the simple geometries being considered in the present work they are sufficiently flexible. A wide range of surfaces can be obtained by varying the location and number of control points.

DOI: 10.1002/fld

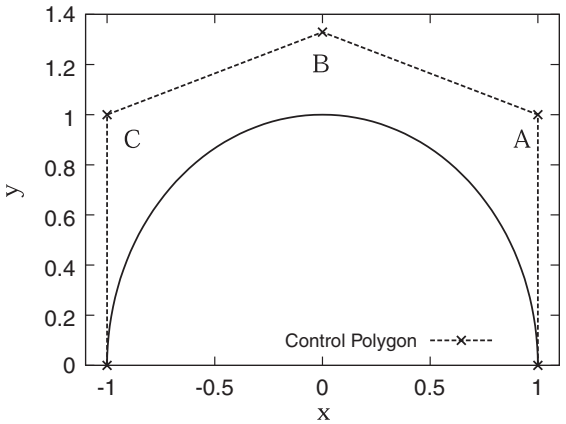

Figure 2. Parametrization of a curve using 4th order Bézier curves with five control points: A, B and C are the control points whose coordinates are used as design variables.

In the Bézier representation the coordinates, $\mathbf{x}$, of the points lying on the curve are given as

$$\mathbf{x}(t) = \sum_{i=0}^{n} \mathbf{P}_i B_i^n(t) \tag{21}$$

where B_i^n are the Bernstein polynomials, n the degree and $t \in [0, 1]$. $\mathbf{P}_i$ are the location of the control points. In the present work 4th order Bézier curves with five control points are utilized to model the surface. The two endpoints are frozen and the x and y coordinates of the remaining three control points are used as design variables. Figure 2 shows the control polygon of the Bézier curve and a typical resulting surface. The example shown in the figure is that of obtaining an approximation to one-half of a circle. In the optimization cycle each design variable is allowed to change between a lower and an upper bound that is specified *a priori*. The purpose of using a bound is twofold: to restrict the obtained shapes and to avoid unacceptable distortion of the grid. The latter can be relaxed by utilizing remeshing. However, that approach has not been undertaken in the present work.

5. VALIDATION

5.1. Accuracy of gradients

To study the accuracy of the gradients obtained by the continuous adjoint method, they are compared with those computed from a simple finite difference method. The objective function, defined as $I_c = -\frac{1}{2}C_l^2$, allows one to search for a shape that yields maximum lift coefficient. The stencil used to compute the gradients using the finite difference method is given as

$$\frac{\mathrm{d}I_c}{\mathrm{d}\boldsymbol{\beta}} = \frac{I_c(\boldsymbol{\beta} + \Delta\boldsymbol{\beta}) - I_c(\boldsymbol{\beta})}{\Delta\boldsymbol{\beta}} \tag{22}$$

Here, $\boldsymbol{\beta}$ are the design parameters. The choice of the step size, $\Delta\boldsymbol{\beta}$, plays an important role in determining the gradients using the finite difference method. A large value of $\Delta\boldsymbol{\beta}$ leads to large

DOI: 10.1002/fld

truncation error while a very small value can cause round-off error. As is seen from Equation (22), the gradient evaluation *via* a finite difference method for each design parameter requires two function evaluations. This means that the flow needs to be computed twice: for the shape parameter and its perturbed value. In the present case, there are six design parameters $[(x_A, y_A), (x_B, y_B), (x_C, y_C)]$. This leads to six gradients to be evaluated which, therefore, require seven evaluations of the flow field at each iteration of the optimization cycle. The computation of the gradients by the continuous adjoint method is carried out by using Equation (10). The gradient, $\partial I/\partial \boldsymbol{\beta}$ in this case, is the gradient of the augmented objective function. Unlike the finite difference methods, $\partial I/\partial \boldsymbol{\beta}$ requires only one evaluation of the flow and the adjoint variables irrespective of the number of design parameters. The cost of the computation of adjoint variables is smaller than that of the flow because the former are a solution to a linear set of equations. As the number of design variables becomes larger the adjoint method becomes more economical compared to the finite difference method. A finite difference approach, as described by Soto and Lohner [22], is utilized to calculate the gradient from Equation (10). They have also proposed the use of an incomplete-gradient formulation that further reduces the cost of the procedure by making certain approximations. However, that method has not been used in the present work.

The derivatives of the lift coefficient with respect to the coordinates of the control points obtained by using the continuous adjoint method and finite differences, with different step size $\Delta\boldsymbol{\beta}$, given by Equation (22), are plotted in Figure 3. For $\Delta\boldsymbol{\beta}$ of the order of 10^{-3} to 10^{-6} the results from finite differences are virtually independent of the step size. However, the round-off error becomes significant for $\Delta\boldsymbol{\beta}$ smaller than 10^{-6}. For example, the divergence of results obtained with $\Delta\boldsymbol{\beta} = 10^{-7}$ is clearly seen in Figure 3. For $\Delta\boldsymbol{\beta} = 10^{-8}$ (not shown here, as some of them lie out of the window) the gradients obtained are even more different and some, with incorrect sign. For computations in double precision arithmetic, $\Delta\boldsymbol{\beta} = 10^{-6}$ appears to be a good choice for step size. Reasonably good match between the gradient values computed from the finite differences and continuous adjoint method is observed from Figure 3. This increases the confidence in the formulation and the present implementation of the computation of gradient using the adjoint method.

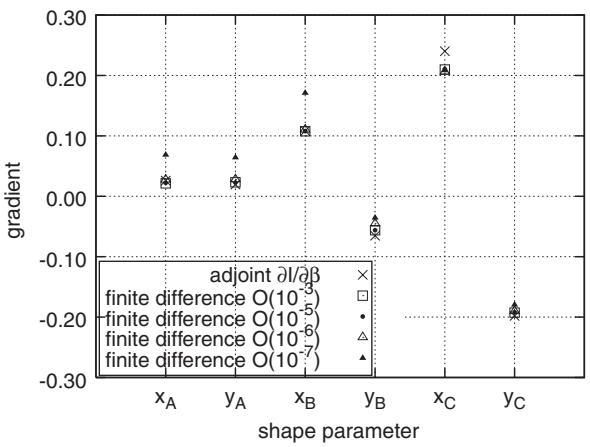

Figure 3. Comparison of derivatives obtained using the continuous adjoint method with finite differences.

DOI: 10.1002/fld

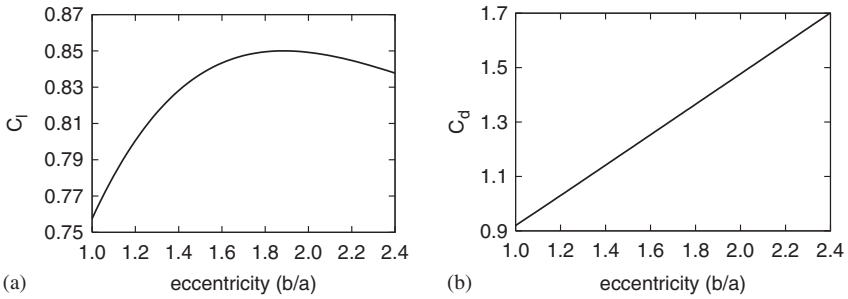

Figure 4. $Re = 25$ flow past an elliptical bump: variation of the lift and drag coefficients with eccentricity b/a of the ellipse.

5.2. $Re = 25$ *flow past an elliptical bump*

The formulation for optimization and its implementation is further validated *via* two tests involving flow past a bump modelled by one-half of the ellipse. The eccentricity, b/a, of the ellipse is used as the design variable. Here, $2a$ and $2b$ are the major and minor axis of the ellipse, respectively. First, computations are carried out for various eccentricity ratios of the bump. The Reynolds number based on the major axis and the free-stream speed is 25. The computations are carried out by fixing the chord of the bump, $2a$, and varying its height, b. Figure 4 shows the variation of the lift and drag coefficients with b/a. The lift coefficient first increases with increase in b/a and then decreases. A local maxima occurs at $b/a \sim 1.8$ and the corresponding lift coefficient is 0.85. As expected, the drag coefficient of the bump increases with increase in its height. These curves are utilized to test the proposed formulation and its implementation. Two test cases are presented. The first one involves determining the height of the bump for which the lift coefficient achieves a maxima. The second test is an inverse problem where the aim is to realize a shape with a specified value of the drag coefficient. These two test problems also serve the purpose of validating the choice of objective functions for carrying out the optimization.

5.2.1. Maximization of the lift coefficient. The goal is to determine the eccentricity of the elliptical bump that results in maximum lift coefficient. To this extent, the objective function is defined as $I_c = -\frac{1}{2}C_l^2$ where C_l is the lift coefficient. There is only one shape parameter in this case: $\beta = b/a$. The computations begin with an initial shape that corresponds to a half cylinder ($b/a = 1$). The lift coefficient for the initial shape is 0.76. The outer boundary of the computational domain is a rectangle which is 60 units long and 20 units high. The finite element mesh consists of 7631 nodes and 14 600 triangular elements. There are 80 nodes on the surface of the bump. A close-up view of the mesh is shown in Figure 5. Figure 6 shows the iteration histories of the lift coefficient, gradient and the eccentricity of the ellipse for the optimization cycle starting from a semi-circular bump. The maximum lift coefficient achieved is 0.85 and the corresponding eccentricity is 1.8. Although the solution does not seem to change much after three iterations, another three iterations are needed to reduce the gradient, $\partial I/\partial\beta$, below the threshold value of 1×10^{-9} that is specified as the convergence criterion. The optimal value of b/a for maximum C_l, from this test, is identical to the one shown in Figure 4. The C_l value from the two sets of computations is also the same. This example demonstrates the ability of the proposed formulation and its implementation to locate the correct maxima. Figure 6(d) shows the initial and the optimal shape. The flow and the adjoint

DOI: 10.1002/fld

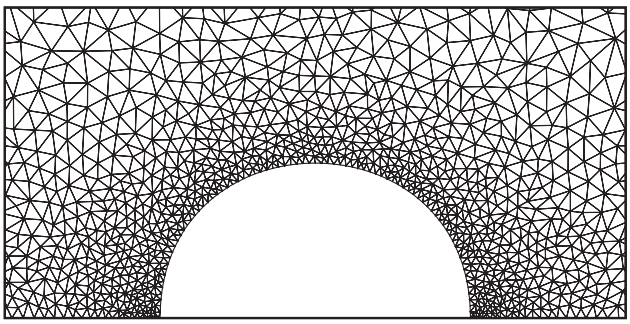

Figure 5. $Re = 25$ flow past an elliptical bump: close-up view of the mesh for the initial shape. The mesh consists of 7631 nodes and 14 600 triangular elements with 80 nodes on the surface.

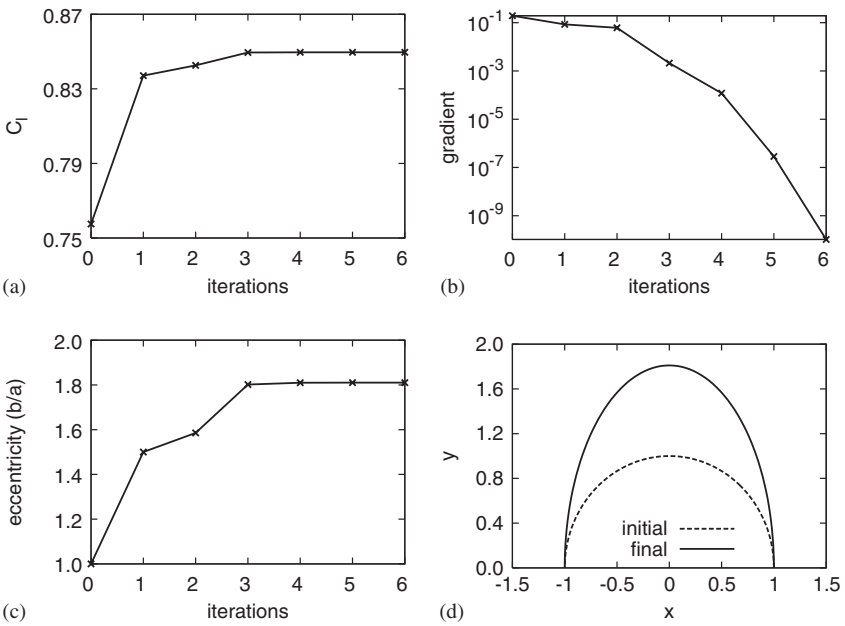

Figure 6. Maximization of C_l for the $Re = 25$ flow past an elliptical bump: iteration histories of the: (a) lift coefficient; (b) gradient; and (c) eccentricity. The initial and final shapes are shown in (d).

field for the optimal geometry are shown in Figures 7(a) and (b), respectively. As expected, the flow is associated with a wake that includes a region of recirculating flow. The adjoint velocity is non-zero mostly close to the body and has relatively small value away from the body.

5.2.2. Inverse design for a specified drag coefficient. The objective here is to determine the eccentricity of the bump that results in a specified value of the drag coefficient. This is an example of an inverse design problem where the shape or surface of a body which satisfies a desired

DOI: 10.1002/fld

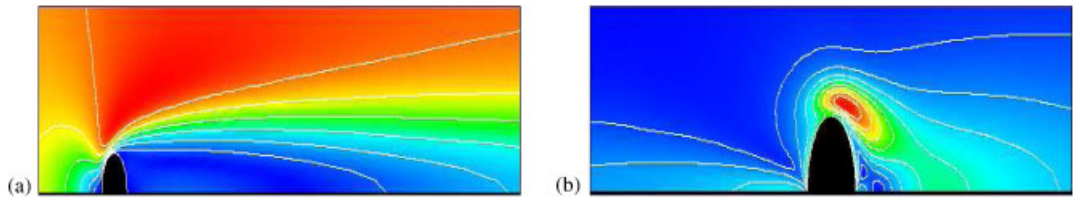

Figure 7. Maximization of C_l for the $Re = 25$ flow past an elliptical bump: (a) magnitude of the flow; and (b) adjoint velocity fields for the optimal shape.

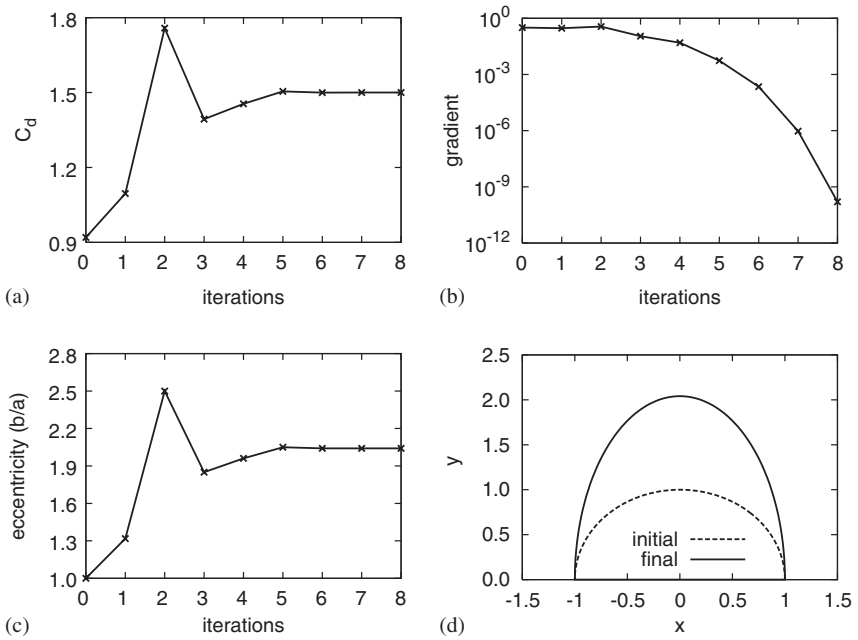

Figure 8. Inverse design for $C_d = 1.5$ for the $Re = 25$ flow past an elliptical bump: iteration histories of the: (a) drag coefficient; (b) gradient; and (c) eccentricity. The initial and final shapes are shown in (d).

objective is to be determined. The objective function for this problem is defined as

$$I_c = \tfrac{1}{2}(C_d - C_d^0)^2 \tag{23}$$

where C_d^0 is the desired drag coefficient. In the present case it is chosen as 1.5. The computations begin with a shape that corresponds to a half cylinder ($b/a = 1$). The drag coefficient for this initial configuration is 0.9. Figures 8(a)–(c) show the iteration histories of the drag coefficient, gradient and the eccentricity. A reasonably accurate solution is available after five iterations. However, it takes eight iterations for the gradient to reduce below the threshold value of 1×10^{-9} specified for convergence. The eccentricity for the converged solution is 2.04. This value is in excellent agreement with the value of b/a from Figure 4(b) that results in $C_d = 1.5$.

The initial and the final shapes of the bump are shown in Figure 8(d).

DOI: 10.1002/fld

6. RESULTS

Having validated the formulation and implementation on a flow with one shape parameter, the number of shape parameters of the bump is now relaxed. For all the flows presented, the Reynolds number based on the free-stream speed and the chord of the bump is 25. The boundary conditions, extent of computational domain and the finite element mesh are same as described earlier.

6.1. Drag minimization

To determine the shape of the bump that minimizes the drag coefficient the objective function is defined as

$$I_c = \tfrac{1}{2} C_{\mathrm{d}}^2 \tag{24}$$

The computations begin with an initial shape that is an approximation to one-half of a cylinder as shown in Figure 2. The drag coefficient for this initial shape is 0.9. Of the six design variables three reach their specified lower bound. Figure 9(a) shows the iteration history of the drag coefficient. As expected, the optimal shape is almost a flat surface. The final geometry is shown in Figure 9(b). The drag coefficient of the final geometry is ~ 0.3. Figure 10 shows the flow and adjoint velocity magnitude fields for the final shape. Computations with different initial conditions lead to the same shape and final drag coefficient.

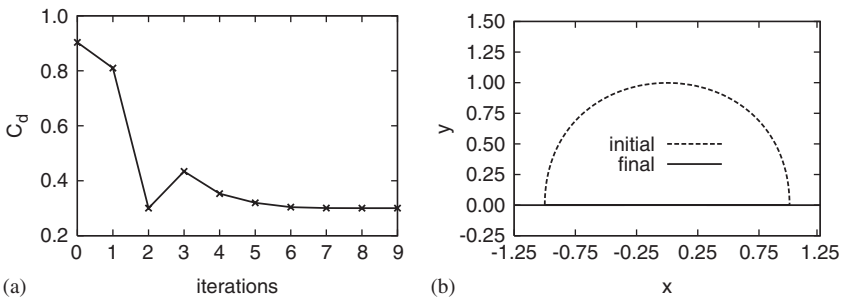

Figure 9. Minimization of the drag coefficient of a bump modelled by a 4th order Bézier curve: (a) iteration history of the drag coefficient; and (b) initial and the final shapes.

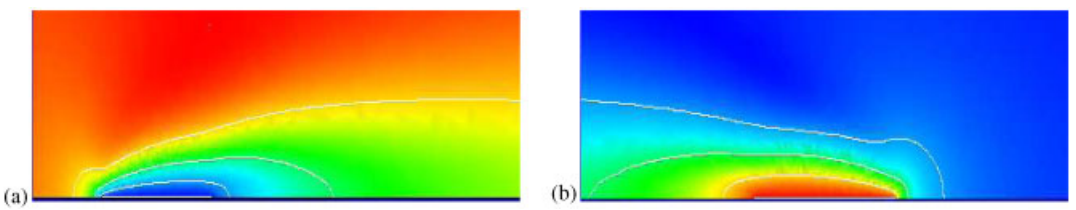

Figure 10. Minimization of the drag coefficient of a body: (a) magnitude of the velocity; and (b) adjoint velocity field for the final shape.

DOI: 10.1002/fld

6.2. *Inverse design for a specified lift coefficient ($C_l = 0.1$)*

The goal here is to determine the shape that yields a lift coefficient of 0.1. The objective function is defined as

$$I_c = \tfrac{1}{2}(C_l - C_l^0)^2 \tag{25}$$

where C_l^0 is the desired lift coefficient. Many shapes that satisfy Equation (25) are possible. To investigate this possibility computations are carried out with seven different initial shapes as shown in Figure 11. Each of these shapes is identified by an alphabet ($a - g$). Table I lists the drag and lift coefficients for these shapes. The final shape for the converged solution obtained from each of the initial shapes ($a - g$) is shown in Figure 12. Each of these shapes results in $C_l = 0.1$. However, the drag coefficient for all these shapes is different and listed in Table II. As can be seen, the shapes shown in Figure 12 are quite different. They have different heights and some of them are associated with an overhang on either side of $x = \pm 1$. One example of such a case with an upstream overhang is the geometry obtained with the initial guess a. In all the cases, the aerodynamic coefficients are computed based on the length of the bump along the x-axis.

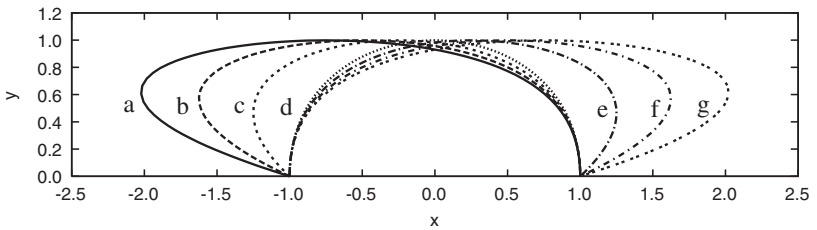

Figure 11. Inverse design for a specified lift coefficient: initial shapes of the bump.

Table I. Inverse design for a specified lift coefficient: drag and lift coefficients for the initial shapes.

Shape	*a*	*b*	*c*	*d*	*e*	*f*	*g*
C_d	0.9088	0.8934	0.9041	0.9033	0.8814	0.8655	0.9378
C_l	1.545	1.3199	1.057	0.7663	0.7541	0.7524	0.7622

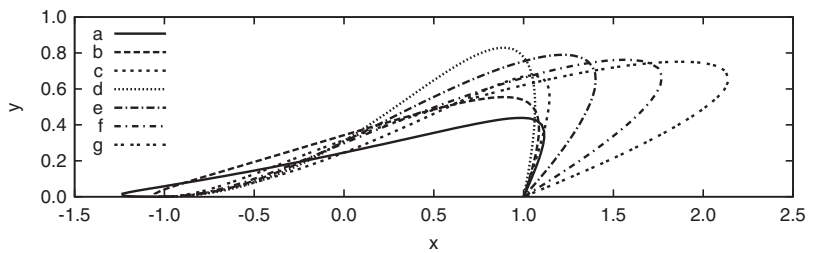

Figure 12. Inverse design for $C_l = 0.1$: final shape of the bump obtained with different initial guesses.

DOI: 10.1002/fld

Table II. Inverse design for $C_l = 0.1$: drag coefficient of the final shape obtained with different initial shapes of the bump.

Shape	*a*	*b*	*c*	*d*	*e*	*f*	*g*
C_d	0.6077	0.6742	0.4806	0.7272	0.6761	0.6542	0.7559

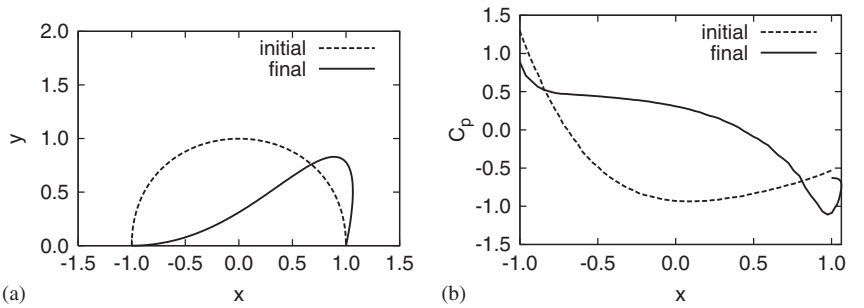

Figure 13. Inverse design for $C_l = 0.1$: (a) the final and initial shape-*d*; and (b) variation of C_p on the surface of the bump.

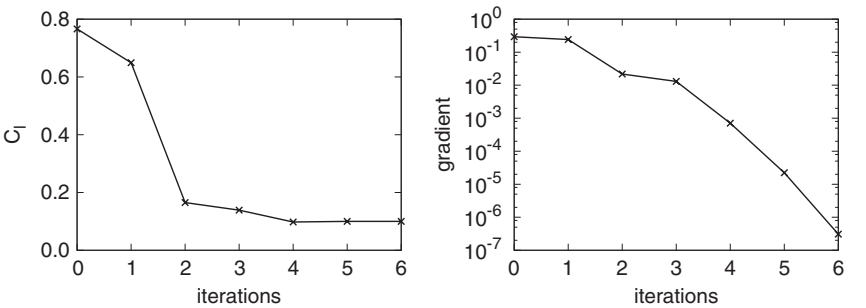

Figure 14. Inverse design for $C_l = 0.1$: iteration histories of the lift coefficient and its gradient for the computations with the initial shape-*d*.

Figure 13(a) shows the initial and the final shape of the surface obtained with the initial guess *d*. The comparison of the variation of the C_p distribution on the surface of the bump for the initial and final shape is shown in Figure 13(b). From Tables I and II it can be seen that compared to the final shape all the initial shapes are associated with larger value of C_l. This is consistent with the variation of the C_p distribution on the surface of the bump. The initial geometry is associated with a larger suction on its surface and, therefore, a larger value of C_l. Figure 14 shows the iteration histories of the lift coefficient and the gradient of the objective function for the initial shape *d*. The magnitude of the velocity field and the corresponding adjoint velocity field for the final geometry are shown in Figure 15. As was also noted earlier, the variations in the adjoint field are mostly seen close to the body. This example demonstrates the usefulness of the present method in exploring

DOI: 10.1002/fld

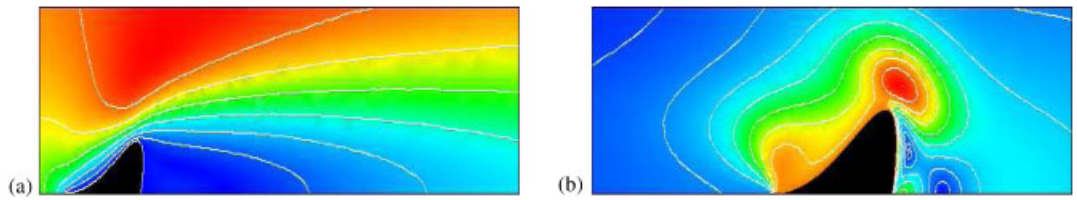

Figure 15. Inverse design for $C_l = 0.1$: (a) magnitude of the flow; and (b) adjoint velocity fields for the final shape obtained with the initial shape-*d*.

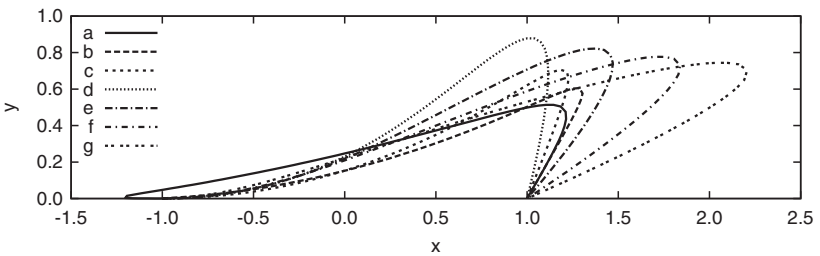

Figure 16. Minimization of the lift coefficient: final shape of the bump with $C_l = 0$ obtained with different initial guesses.

several shapes/designs for a given objective function. It may then be possible to choose the one that further satisfies some more desirable constraints.

6.3. *Minimization of the magnitude of lift coefficient*

In continuation with the previous section, the objective in this case is to minimize the lift on the bump. A trivial solution is the flat plate that results in zero lift. The motivation here is to determine other shape(s) that also result in zero lift. Three cases of minimizing the magnitude of lift coefficient are considered: (1) no constraints, (2) a geometric constraint and (3) a geometric constraint and an inverse constraint on the drag coefficient. The effect of progressively increasing the constraints, on the resulting shapes, is studied.

6.3.1. Case 1: no constraints. The objective function is defined as

$$I_c = \tfrac{1}{2} C_l^2 \tag{26}$$

This objective function is expected to drive the solution to $C_l = 0$. In case, such a geometry does not exist the final solution will be driven to a geometry that yields a local minima of C_l. The computations are initiated with several geometries as the initial guess. They are shown in Figure 11. Figure 16 shows the optimal shapes obtained with the various initial guesses. All these shapes yield $C_l = 0$. These shapes are quite similar to the ones obtained for $C_l = 0.1$ and are shown in Figure 12. The drag coefficient and area under the bump are different for all the shapes. The top row in Table III lists the drag coefficients associated with the various shapes.

DOI: 10.1002/fld

Table III. Minimization of the lift coefficient: drag coefficient of the various shapes of the bump with $C_l = 0$ obtained with different initial guesses.

Shape	*a*	*b*	*c*	*d*	*e*	*f*	*g*
Case-1	0.4911	0.4323	0.4571	0.7557	0.6849	0.6523	0.7572
Case-2	—	—	1.077	1.137	1.029	0.908	0.916

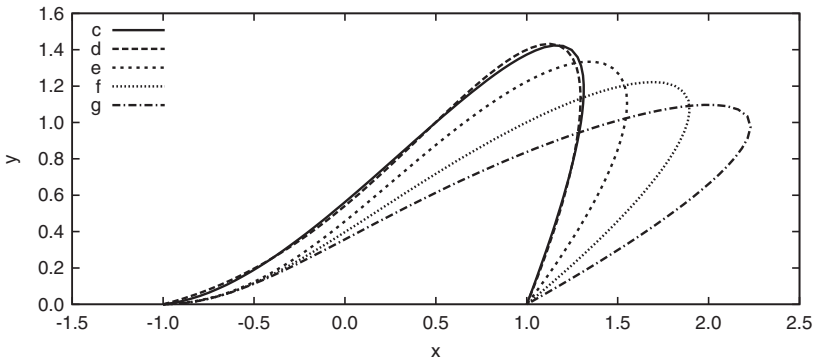

Figure 17. Minimization of the lift coefficient with a constraint on the volume of the bump: final shape of the bump with $C_l = 0$ obtained with different initial guesses.

6.3.2. Case 2: with geometric constraint. In the previous section it was observed that many shapes that lead to $C_l = 0$ are possible. However, they are associated with different volumes (per unit depth) and C_d. The effect of further constraining the design space on the multiplicity of solutions is investigated. To begin with a geometric constraint is specified. It is possible to include various types of geometric constraints such that the final design has specific geometric properties like volume, height, etc. In this exercise the lift coefficient is minimized while conserving the volume enclosed by the bump. The objective function is defined as

$$I_c = \tfrac{1}{2}C_l^2 + \tfrac{1}{2}\alpha(V - V^0)^2 \tag{27}$$

where V^0 is the desired volume. The factor α is the relative weight of the volume constraint with respect to the constraint on the lift. In the present computations α is assigned the value 1.0. V^0 is the volume of the half cylinder ($= \pi/2$). Computations are carried out with several geometries shown in Figure 11 as the initial guess. In this case, the initial shapes *a* and *b* do not lead to any shape that satisfy the desired condition on the volume and lift coefficient. The converged solutions obtained with the other initial guesses are shown in Figure 17. Compared to the shapes in Figure 16 the shapes in the figure look closer to each other. The imposition of the volume constraint brings about significant reduction in the design space. Table III (row 2) lists the drag coefficient associated with the various solutions.

6.3.3. Case 3: with geometric and aerodynamic constraints. To reduce the design space further, an additional constraint is imposed. The objective now is to determine shape(s) that have minimum

DOI: 10.1002/fld

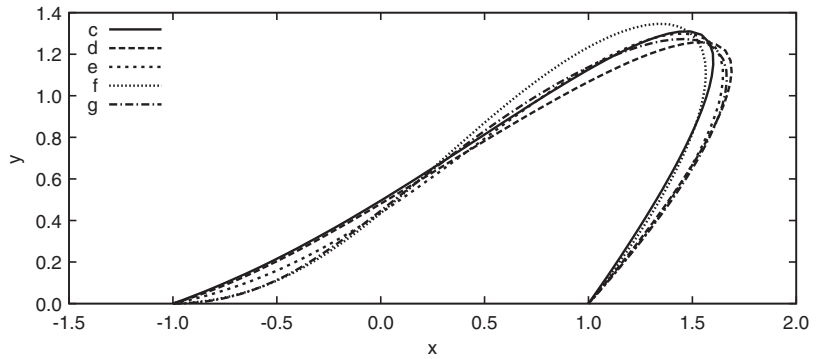

Figure 18. Minimization of the lift coefficient with constraints on the volume of the bump and its drag coefficient: final shape of the bump with $C_l = 0$ and $C_d = 1$ obtained with different initial guesses.

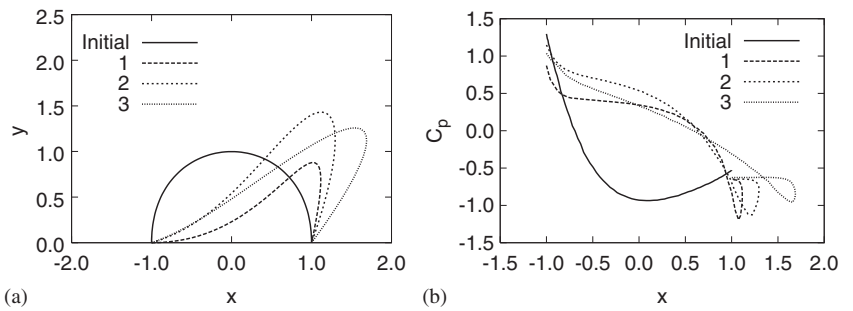

Figure 19. Minimization of the lift coefficient: the final shapes for and initial shape-d and the corresponding C_p distribution on the surface.

lift coefficient such that the resulting bump has a prescribed volume, V^0, and a drag coefficient, C_d^0. The objective function is defined as

$$I_c = \tfrac{1}{2}C_l^2 + \tfrac{1}{2}\alpha(V - V^0)^2 + \tfrac{1}{2}\beta(C_d - C_d^0)^2 \tag{28}$$

where α and β are the relative weightages that can be assigned to the constraints on volume and drag coefficient, respectively. In the present case the various values that are assigned are $\alpha = \beta = 1$, $C_d^0 = 1.0$ and $V^0 = \pi/2$. Computations are carried out with all the geometries shown in Figure 11 as the initial guess. As in the previous case, the initial shapes a and b do not lead to any shape that satisfies the desired conditions on the volume and aerodynamic coefficients. The solutions at the end of the optimization cycle with the other initial shapes are shown in Figure 18. As expected, the solutions from the various initial guesses are closer to each other as compared to the ones obtained with fewer constraints. This shows a reduction in the design space as more constraints are introduced.

Figure 19(a) shows the initial and final shapes for all the three cases obtained with the initial guess d. The corresponding C_p distribution on the surface of the bump is shown in Figure 20(b). Figure 20 shows the iteration histories of the lift coefficient and the gradient of the objective

DOI: 10.1002/fld

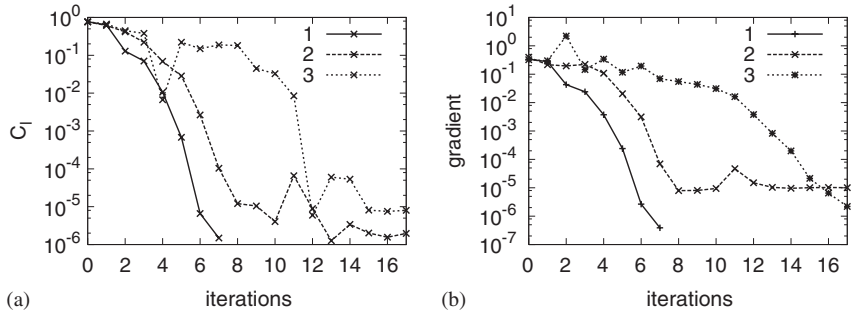

Figure 20. Minimization of the lift coefficient with constraints on the volume of the bump and its drag coefficient: iteration history of the lift coefficient and the gradient.

function. Both, C_l and the gradient converge to near zero values at the end of computation for all the cases that have been studied. It can be observed that as the number of constraints increase, thereby reducing the design space, the optimization cycle requires more iterations to converge.

7. CONCLUDING REMARKS

A continuous adjoint approach for shape optimization in steady low Reynolds number flows has been formulated and implemented. Unlike the flow equations, the equations for the adjoint variables are linear. A stabilized finite element method based on SUPG/PSPG stabilizations has been used to solve, both, the flow and adjoint equations. The L-BFGS algorithm has been used to update the shape parameters. The stopping criterion for the optimization loop is the reduction of the magnitude of the gradient below a certain threshold. Flow past an elliptical bump, with its eccentricity as the only design parameter, is utilized to validate the optimization procedure.

A relatively more complex representation of the bump with 4th order Bézier curves provides the possibility of more design variables to search for more optimal solutions. First, the accuracy of the gradients of the objective function with respect to the shape parameters is validated against a simple finite difference procedure. The computational effort in the evaluation of gradient increases linearly with the number of design variables for the finite difference procedure. This is not so with the adjoint-based method. The number of flow and adjoint field evaluations is independent of the number of design variables. As a result, as the number of design parameters increases the adjoint-based procedure becomes more economical for evaluating the gradients. Results for, both, optimal design and inverse problems are presented. Using different initial shapes, it is possible to obtain multiple shapes that satisfy a given objective function. This is demonstrated for an inverse problem for achieving a certain value of the lift coefficient and also when minimizing it. These shapes, although satisfying the objective function, are associated with different drag coefficient, volume, etc. To constrain the design space, the objective function is augmented with additional constraints on the volume and the drag coefficient of the bump. It is seen that with these constraints the final shapes are very similar to each other. This study demonstrates the usefulness of this tool in obtaining multiple engineering solutions to a given design problem and also providing a framework to impose several constraints simultaneously. Work is in progress to extend this methodology to unsteady flows and apply it to flows at higher Reynolds numbers.

DOI: 10.1002/fld

REFERENCES

1. Nocedal J, Wright SJ. *Numerical Optimization*. Springer Series in Operations Research. Springer: New York, 1999.
2. Squire W, Trapp G. Using complex variables to estimate derivatives of real functions. *SIAM Review* 1998; **40**(1):110–112.
3. Newman III JC, Whitefield DL, Anderson WK. A step-size independent approach for multidisciplinary sensitivity analysis. *Journal of Aircraft* 2003; **40**(3):566–573.
4. Burg COE, Newman III JC. Computationally efficient, numerical exact design derivatives via the complex Taylor's series expansion method. *Computers and Fluids* 2003; **32**:373–383.
5. Martins JPRA, Kroo IM, Alonso JJ. An automated method for sensitivity analysis using complex variables. *AIAA Paper 000-0689*, 2000.
6. Newman JC III, Taylor AC III, Barnwell RC, Newman PA, Hou GJW. Overview of sensitivity analysis and shape optimization for complex aerodynamic configurations. *Journal of Aircraft* 1999; **36**(1):87–96.
7. Hou GJW, Maroju V, Taylor III VC, Korivi M, Newman PA. Transonic turbulent airfoil design optimization using automatic differentiation in incremental iterative form. *AIAA Paper 1995-1692*.
8. Sherman LL, Taylor III AC, Green LL, Newman PA, Hou GJW, Korivi M. First and second order aerodynamic sensitivity derivatives via automatic differentiation with incremental iterative methods. *Journal of Computational Physics* 1994; **129**:307–331.
9. Hou GJW, Sheen JS, Chuang CH. Shape sensitivity analysis and design optimization of linear thermoelastic solids. *AIAA Journal* 1992; **30**(2):528–537.
10. Giles MB, Pierce NA. An introduction to the adjoint approach to design. *Flow, Turbulence and Combustion* 2000; **65**:393–415.
11. Gunzburger MD. Sensitivities, adjoints and flow optimization. *International Journal for Numerical Methods in Fluids* 1999; **31**:53–78.
12. Pironneau O. On optimum profiles in Stokes flow. *Journal of Fluid Mechanics* 1973; **59**:117–128.
13. Pironneau O. On optimum design in fluid mechanics. *Journal of Fluid Mechanics* 1974; **64**:97–110.
14. Jameson A. Aerodynamic design via control theory. *Journal on Scientific Computing* 1988; **59**:117–128.
15. Abraham FV. Stabilized finite element solution of optimal control problems in computational fluid dynamics. *Ph.D. Dissertation*, Mechanical Engineering and Materials Science, Rice University, 2004.
16. Nadarajah S, Jameson A. Studies of the continuous and discrete adjoint approaches to automatic aerodynamic optimization. *AIAA Paper 2000-0667*, 2000.
17. Reuthers J, Jameson A, Farmer J, Martinelli L, Saunders D. Aerodynamic shape optimization of complex aircraft configurations via adjoint formulations. *AIAA Paper 96-0094*, 1996.
18. Kyle Anderson W, Venkarakrishnan V. Aerodynamic design optimization on unstructured grids with a continuous adjoint formulations. *AIAA Paper 97-0643*, 1997.
19. Brezillion J, Gauger NR. 2D and 3D aerodynamic shape optimization using the adjoint approach. *Aerospace Science and Technology* 2004; **8**:715–727.
20. Kim S, Alonso JJ, Jameson A. Two-dimensional high lift aerodynamic optimization using the continuous adjoint method. *AIAA Paper 2000-4741*, 2000.
21. Soto O, Lohner R, Yang C. An adjoint-based design methodology for CFD problems. *International Journal of Numerical Methods for Heat and Fluid Flow* 2004; **14**:734–759.
22. Soto O, Lohner R. CFD shape optimization using an incomplete-gradient adjoint formulation. *International Journal for Numerical Methods in Engineering* 2001; **51**:735–753.
23. Elliot J, Perraire J. Practical three-dimensional design and optimization using unstructures meshes. *AIAA Journal* 1997; **35**:1479–1485.
24. Anderson W, Bonhaus D. Airfoil design on unstructured grids for turbulent flows. *NASA TM 112867*, 1997.
25. Gunzburger Md. Adjoint equation-based methods for control problems in incompressible, viscous flows. *Flow, Turbulence and Combustion* 2000; **65**:249–272.
26. Mohammadi B, Pirroneau O. Shape optimization in fluid mechanics. *Annual Review of Fluid Mechanics* 2004; **36**:255–279.
27. Abraham F, Behr M, Heinkenschloss M. Shape optimization in steady blood flow: a numerical study of non-Newtonian effects. *Computer Methods in Biomechanics and Biomedical Engineering* 2005; **8**:127–137.
28. Abraham F, Behr M, Heinkenschloss M. Shape optimization in unsteady blood flow: a numerical study of non-Newtonian effects. *Computer Methods in Biomechanics and Biomedical Engineering* 2005; **8**:201–212.

DOI: 10.1002/fld

29. Yagi H, Kawahara M. Shape optimization of a body located in low Reynolds number flow. *International Journal for Numerical Methods in Fluids* 2005; **48**:819–833.
30. Okumura H, Kawahara M. Shape optimization of a body located in incompressible Navier–Stokes flow based on optimal control theory. *Computer Modelling in Engineering and Sciences* 2000; **1**:71–77.
31. Tezduyar TE, Mittal S, Ray SE, Shih R. Incompressible flow computations with stabilized bilinear and linear equal order interpolation velocity pressure elements. *Computer Methods in Applied Mechanics and Engineering* 1992; **95**:221–242.
32. Byrd RH, Lu P, Nocedal J, Zhu C. A limited memory algorithm for bound constrained optimization. *SIAM Journal on Scientific Computing* 1995; **16**:1190–1208.
33. Farin G. *Curves and Surfaces for Computer Aided Geometric Design. A Practical Guide*. Academic Press: New York, 1990.
34. Tezduyar TE, Behr M, Mittal S, Johnson AA. Computation of unsteady incompressible flows with the finite element methods—space–time formulations, iterative strategies and massively parallel implementations. In *New Methods in Transient Analysis*, Smolinski P, Liu WK, Hulbert G, Tamma K (eds). AMD-vol. 143. ASME: New York, 1992; 7–24.

DOI: 10.1002/fld